Evaluation of the angular spectrum approach for simulations of near-field pressures

Xiaozheng Zeng[a] and Robert J. McGough[b]
Department of Electrical and Computer Engineering, Michigan State University, East Lansing, Michigan 48824, USA

(Received 3 May 2007; revised 15 October 2007; accepted 18 October 2007)

The implementation of the angular spectrum approach based on the two-dimensional fast Fourier transform is evaluated for near-field pressure simulations of square ultrasound transducers, where the three-dimensional pressure field is calculated from the normal velocity distribution on the transducer surface. The pressure field is propagated in the spatial frequency domain with the spatial propagator or the spectral propagator. The spatial propagator yields accurate results in the central portion of the computational grid while significant errors are produced near the edge due to the finite extent of the window applied to the spatial propagator. Likewise, the spectral propagator is inherently undersampled in the spatial frequency domain, and this causes high frequency errors in the computed pressure field. This aliasing problem is alleviated with angular restriction. The results show that, in nonattenuating media, the spatial propagator achieves smaller errors than the spectral propagator after the region of interest is truncated to exclude the windowing error. For pressure calculations in attenuating media or with apodized pistons as sources, the spatial and spectral propagator achieve similar accuracies. In all simulations, the angular spectrum calculations with the spatial propagator take more time than calculations with the spectral propagator.
 [DOI: 10.1121/1.2812579]

PACS number(s): 43.38.Hz, 43.20.El, 43.20.Rz, 43.40.Rj [TDM] Pages: 68–76

I. INTRODUCTION

The angular spectrum approach describes the diffraction of acoustic waves from finite apertures by superposing plane waves traveling in different directions[1] and propagating these components in the spatial frequency domain. As opposed to integral approaches that calculate the field at each observation point, the angular spectrum approach computes the pressure field in successive planes with a two-dimensional (2D) fast Fourier transform (FFT), which speeds up these calculations significantly. The angular spectrum approach uses either the normal particle velocity or the pressure as the source, and then the spectral propagator function or the 2D Fourier transform of the spatial propagator is multiplied by the source in the spatial frequency domain to simulate the propagation of acoustic waves. The spectral propagator is described as an analytical function,[2–9] whereas the spatial propagator is calculated analytically and then transformed into the spatial frequency domain with a 2D FFT.[10–12]

The spectral propagator is frequently applied to the angular spectrum approach. Williams[13,14] analyzes the effect of the windowing function, the aliasing errors due to the lack of spectral samples, and the singularity of the spectral propagator. Orofino[3,4] discusses the spatial sampling rate and the angular resolution. Christopher and Parker[10] and Wu *et al.*[6–8] both investigate an angular restriction technique to reduce the aliasing error due to undersampling of the spectral propagator, and Wu and co-workers derive the optimal bandwidth of a low-pass spatial filter that truncates the undersampled spatial frequencies. The spatial propagator is less frequently employed due to the additional 2D FFT calculation required in each plane.

A better understanding of the trade-offs between the spectral propagator and the spatial propagator in terms of numerical accuracy and computational time is clearly needed. Christopher and Parker[10] claim that the spatial propagator produces more accurate results in the context of on-axis simulations for axisymmetric radiators using the fast Hankel transform. However, comparisons relative to a standard reference are not evaluated for the off-axis case. Zemp[12] argues that the spectral propagator is superior to the spatial propagator when the spatial sampling is coarser than $\lambda/2$, which is applicable only in the far field. In many applications, the region of interest is the near field, and comparisons with higher sampling rates are desired.

This paper thoroughly compares the spatial propagator and the spectral propagator for angular spectrum calculations in a homogeneous three-dimensional (3D) domain. The pressure field from a square piston with uniform particle velocity distribution is computed with the fast near-field method[15] as the reference, and for an apodized particle velocity distribution, the Rayleigh–Sommerfeld integral is the reference. The errors in the computed pressure field for the angular spectrum approach using the spatial propagator and the spectral propagator (with and without angular restriction) are then compared. First, the role of angular restriction in angular spectrum calculations with the spectral propagator is established. Second, the errors generated in the edge of the computational grid specific to the spatial propagator are identified and explained. Third, the frequency filtering effect of attenuating media is shown to eliminate the need for angular

[a]Electronic mail: zengxiao@msu.edu
[b]Electronic mail: mcgough@egr.msu.edu

restriction. Fourth, a similar effect is demonstrated for velocity source apodization. The results show that for the uniformly excited source in nonattenuating media, the spatial propagator yields smaller errors in the central portion of the grid, whereas the spectral propagator outperforms the spatial propagator in attenuating media or for an apodized source by achieving similar accuracy in a larger region in less time.

II. THEORY

A. The Rayleigh–Sommerfeld integral

For a planar radiator mounted on an infinite rigid baffle, the radiated time-harmonic pressure field is represented by the Rayleigh–Sommerfeld diffraction integral,[1]

$$p(\mathbf{r},t) = j\rho ck e^{j\omega t} \int_{\mathbf{S}'} u(\mathbf{r}') \frac{e^{-jk|\mathbf{r}-\mathbf{r}'|}}{2\pi|\mathbf{r}-\mathbf{r}'|} d\mathbf{S}', \tag{1}$$

where ρ and c represent the medium density and the speed of sound, respectively, k is the acoustic wavenumber, ω is the driving frequency, u is the distribution of the normal velocity on the radiator with surface area $\mathbf{S}'$, j is $\sqrt{-1}$, and $|\mathbf{r}-\mathbf{r}'|$ is the distance between the source and the observation coordinates. Numerical implementations of Eq. (1) often divide the radiator aperture into point sources and superpose the results.[16] This approach is especially time-consuming in the near-field region due to the large number of abscissas required for the convergence of the 2D integral and the numerical singularity on the piston surface. Equation (1) calculates the near-field reference pressure for radiators with nonuniform velocity distributions, whereas significantly faster approaches such as the fast near-field method[15] are available for pressure calculations with uniform velocity distributions.

B. The fast near-field method

The fast near-field method[15] is a rapidly converging one-dimensional (1D) integral approach that is analytically equivalent to Eq. (1) for a uniform surface velocity u_0. The fast near-field method formula for the near-field pressure is

$$\begin{aligned} p(x,y,z,t) = j\rho c u_0 e^{j\omega t} \frac{1}{2\pi} \Bigg(& s_1 \int_{-l_1}^{l_2} \frac{e^{-jk\sqrt{z^2+\sigma^2+s_1^2}} - e^{-jkz}}{\sigma^2+s_1^2} d\sigma \\ & + l_1 \int_{-s_1}^{s_2} \frac{e^{-jk\sqrt{z^2+\sigma^2+l_1^2}} - e^{-jkz}}{\sigma^2+l_1^2} d\sigma \\ & + s_2 \int_{-l_1}^{l_2} \frac{e^{-jk\sqrt{z^2+\sigma^2+s_2^2}} - e^{-jkz}}{\sigma^2+s_2^2} d\sigma \\ & + l_2 \int_{-s_1}^{s_2} \frac{e^{-jk\sqrt{z^2+\sigma^2+l_2^2}} - e^{-jkz}}{\sigma^2+l_2^2} d\sigma \Bigg), \end{aligned} \tag{2}$$

where $s_1=a-x$, $l_1=b-y$, $s_2=a+x$, $l_2=b+y$, σ is the 1D variable of integration, and a and b present the half-width and the half-height of the rectangular piston, respectively. This approach eliminates the singularities that are encountered in numerical evaluations of the Rayleigh–Sommerfeld integral and the impulse response.[17]

C. The angular spectrum approach

Equation (1) is a 2D convolution, where the source is located in the $z=0$ plane such that

$$p(x,y,z,t) = j\rho ck e^{j\omega t} u(x,y) \otimes h_u(x,y,z), \tag{3}$$

and the *spatial propagator* is defined as

$$h_u(x,y,z) = \frac{e^{-jkr}}{2\pi r}, \tag{4}$$

where $r=\sqrt{x^2+y^2+z^2}$ is the distance from the origin to an arbitrary field point. Applying a 2D Fourier transform to both sides of Eq. (3) transforms the formula into the spatial frequency domain,

$$P(k_x,k_y,z,t) = j\rho ck e^{j\omega t} U(k_x,k_y) H_u(k_x,k_y,z), \tag{5}$$

where $H_u(k_x,k_y,z)$ is the *spectral propagator*, which is defined as

$$H_u(k_x,k_y,z) = \begin{cases} \dfrac{e^{-jz\sqrt{k^2-k_x^2-k_y^2}}}{j\sqrt{k^2-k_x^2-k_y^2}}, & k_x^2+k_y^2 \leqslant k^2 \\ \dfrac{e^{-z\sqrt{k_x^2+k_y^2-k^2}}}{\sqrt{k_x^2+k_y^2-k^2}}, & k_x^2+k_y^2 > k^2. \end{cases} \tag{6}$$

The Fourier transform decomposes the diffracted wave into the superposition of plane waves, where (k_x,k_y) are the transverse wavenumbers. In the region where $k_x^2+k_y^2 \leqslant k^2$, $H_u(k_x,k_y,z)$ propagates the field in the z direction by applying a complex weight to each plane wave component. In the region where $k_x^2+k_y^2>k^2$, $H_u(k_x,k_y,z)$ exponentially attenuates evanescent waves. The product of the source spectrum $U(k_x,k_y)$ and the propagator function $H_u(k_x,k_y,z)$ describes the spectrum of the propagating wave in an arbitrary plane parallel to the source plane. The pressure distribution is then obtained from the inverse 2D Fourier transform of $P(k_x,k_y,z,t)$.

When the angular spectrum approach calculates pressure fields with the *spatial propagator* $h_u(x,y,z)$,[10–12] the infinite field is truncated in both the x and the y directions so that the extent of each computational plane is $D\times D$. In the simulations that follow, the radiator is a $2a\times 2a$ square piston with $2a<D$. The source plane is illustrated in Fig. 1. The normal particle velocity distribution is defined as $u(x,y)$ within the $2a\times 2a$ area and zero otherwise. With a sample spacing of δ, the $D\times D$ source plane that contains the piston surface is discretized to $N\times N$ grid points, where $N=D/\delta+1$. The field is computed in a discretized grid, and the discrete coordinates are

$$\begin{aligned} x &= m\delta, \quad m = -N/2+1+\phi, \ldots, N/2+\phi, \\ y &= n\delta, \quad n = -N/2+1+\phi, \ldots, N/2+\phi, \end{aligned} \tag{7}$$

$$\phi = \begin{cases} -\dfrac{1}{2} & \text{when } N \text{ is odd}, \\ 0 & \text{when } N \text{ is even}, \end{cases} \tag{8}$$

where ϕ ensures that the grid is symmetric for odd N. For even N, the grid is biased so that points on the central axis

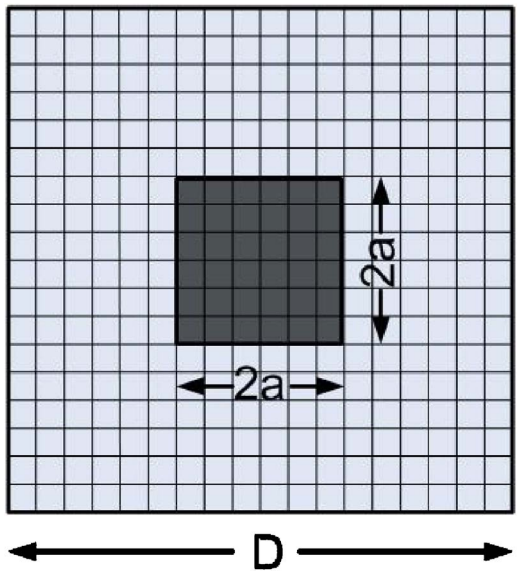

FIG. 1. (Color online) The $D \times D$ source plane consisting of a nonzero normal particle velocity distribution in a $2a \times 2a$ square area on the piston surface. The remaining area is filled with zeros.

are included in the three-dimensional grid. The 2D FFT is then applied to both $h_u(x,y,z)$ and $u(x,y)$, and these are multiplied in the spatial frequency domain. The complex pressure is the inverse 2D FFT of the result.

When the angular spectrum approach calculates pressure fields with the *spectral propagator* $H_u(k_x,k_y,z)$, the spectrum is discretized to an $N \times N$ grid, and the discrete wavenumbers are

$$k_x = m\Delta k, \quad m = -N/2 + 1 + \phi, \ldots, N/2 + \phi,$$

$$k_y = n\Delta k, \quad n = -N/2 + 1 + \phi, \ldots, N/2 + \phi, \tag{9}$$

where the offset ϕ is defined in Eq. (8). The maximum value of k_x is π/δ, the maximum value of k_y is π/δ, and the spectral sample spacing is $\Delta k = 2\pi/(N\delta)$. A large value of N is often required to adequately sample $H_u(k_x,k_y,z)$. The corresponding value of D is therefore significantly larger than $2a$.

D. Angular restriction

The spectral propagator $H_u(k_x,k_y,z)$ encounters problems with rapidly oscillating real and imaginary components as $\sqrt{k_x^2+k_y^2}$ approaches k. In this region, H_u is inherently undersampled, and this undersampling leads to severe aliasing errors.[7] The undersampling can be reduced by increasing N at an expense of increased computational cost. Christopher and Parker[10] and Wu *et al.*[7,8] use a spatial frequency truncation technique as an alternative solution to this problem. This technique reduces the aliasing errors without increasing the size of the computational grid. Spatial frequency truncation is achieved through angular restriction, which applies a spatial low-pass filter to the spectral propagator function H_u, and the cut-off, or angular threshold, is given by[8]

$$k_c = k\sqrt{\frac{D^2/2}{D^2/2 + z^2}}, \tag{10}$$

which specifies a radially symmetric window in 2D. Angular restriction removes the under-sampled angular spectra and prevents the high spatial frequency components from leaking into the propagating field.

E. Attenuation calculations

When the spatial propagator is used in attenuating media, the real-valued wavenumber k in $h_u(x,y,z)$ is replaced by the complex wavenumber $k - j\alpha$, where α is the attenuation coefficient for a particular frequency. For the spectral propagator, $H_u(k_x,k_y,z)$ is multiplied by an exponential term

$$S(k_x,k_y,z) = \exp\left(-\frac{\alpha z k}{\sqrt{k^2 - k_x^2 - k_y^2}}\right), \tag{11}$$

which is a simplified expression that is mathematically equivalent to the trigonometric attenuation term in Eq. (12) of Ref. 10. Within the region where $k_x^2 + k_y^2 \leq k^2$, $S(k_x,k_y,z)$ is analogous to a spatial low-pass filter. As z increases, the peak amplitude of $S(k_x,k_y,z)$ decreases, and the higher spatial frequency components are increasingly attenuated.

F. Error metric

The numerical errors produced by the angular spectrum approach are evaluated with the normalized root mean squared error (NRMSE). This error metric is defined by

$$\mathrm{NRMES} = \frac{\sqrt{\frac{1}{n_x n_y n_z}\sum_{i,j,k} |p^{i,j,k} - p_{\mathrm{ref}}^{i,j,k}|^2}}{\max_{i,j,k}|p_{\mathrm{ref}}^{i,j,k}|}, \tag{12}$$

where the superscripts (i,j,k) represent discrete field points in the computational grid and n_x, n_y, and n_z describe the number of points in each direction. The variable p_{ref} denotes the complex reference pressure, which is computed by the fast near-field method for a piston with uniform normal velocity distribution and by the Rayleigh–Sommerfeld integral for an apodized piston. The variable p is the complex pressure computed by the angular spectrum approach. The root mean squared error is normalized by the global maximum of the 3D reference pressure amplitude.

III. NUMERICAL RESULTS

Simulated pressure fields are generated by a single square piston in a 3D computational grid. The piston, which is 3 cm wide and 3 cm high ($a = 1.5$ cm), is excited at a frequency of 1 MHz. The speed of sound for these simulations is 1500 m/s, so the piston size in wavelength is $20\lambda \times 20\lambda$. The axial grid extends from 0.15 to 30 cm (λ to $2a^2/\lambda$) with an axial sampling interval of 1.5 mm (λ). The maximum transverse extent is $D = 9$ cm (60λ) with a transverse sample spacing of $\lambda = 0.3$ mm ($\lambda/5$), so $N = 301$. The transverse sample spacing is relatively small so that the rapid pressure oscillations are captured in the near field. The spatial propagator and the spectral propagator are both implemented in nonattenuating and attenuating media for a piston

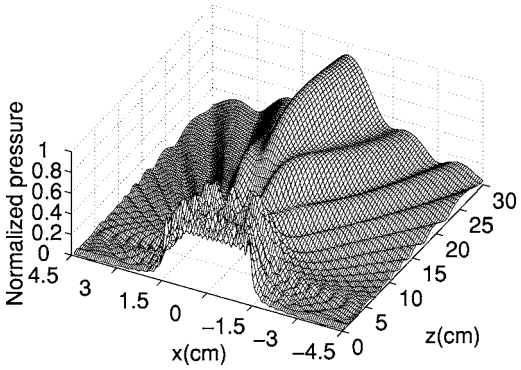

FIG. 2. A two-dimensional cross section of the three-dimensional reference pressure generated by a 3 cm × 3 cm square piston in nonattenuating media. The excitation frequency is 1 MHz, and the normal particle velocity distribution is uniform across the piston surface. The reference pressure is computed with the fast near-field method. The result is normalized to the maximum pressure amplitude computed in the three-dimensional volume.

with uniform normal particle velocity. A quadratically apodized normal velocity distribution is also evaluated in nonattenuating media.

A. Pressure calculations in nonattenuating media for a square piston with uniform normal particle velocity

The reference pressure field generated by the square piston with uniform normal velocity distribution is shown in Fig. 2. The pressure field is evaluated in the $y=0$ plane, and the transverse extent of this plane in both directions is $D=9$ cm. The reference pressure is calculated with the fast near-field method[15] using 100 Gauss abscissas. The reference pressure achieves 11 digits of accuracy throughout the computational grid, where the accuracy is determined by comparing the result to that obtained with 2000 Gauss abscissas. The 3D pressure field is then calculated in successive 9 cm × 9 cm transverse planes using the spectral propagator and the spatial propagator.

Figures 3(a) and 3(b) demonstrate the pressure computed by the spectral propagator without angular restriction and with angular restriction, respectively. The pressure field in Fig. 3(a) contains significant errors due to the aliasing of high spatial frequencies in the spectral propagator, where aliasing is caused by undersampling H_u. In Fig. 3(b), the oscillatory errors are significantly reduced by angular restriction. According to Eq. (10), the angular thresholds at locations $z=10$, 20, and 30 cm are $0.5369k$, $0.3032k$, and $0.2075k$, respectively, where k is the wavenumber. However, ripples still appear in Fig. 3(b) because the spectrum corresponding to intermediate spatial frequencies is also undersampled. Figures 3(a) and 3(b) demonstrate that removing the high spatial frequencies with angular restriction is beneficial for simulations in nonattenuating media, e.g., in water.

Figure 3(c) shows the pressure computed by the spatial propagator without angular restriction. The computed field is smooth everywhere; therefore, angular restriction is not needed for the spatial propagator. In the paraxial region, the pressure field in Fig. 3(c) closely resembles the reference field in Fig. 2. However, starting a certain distance from the

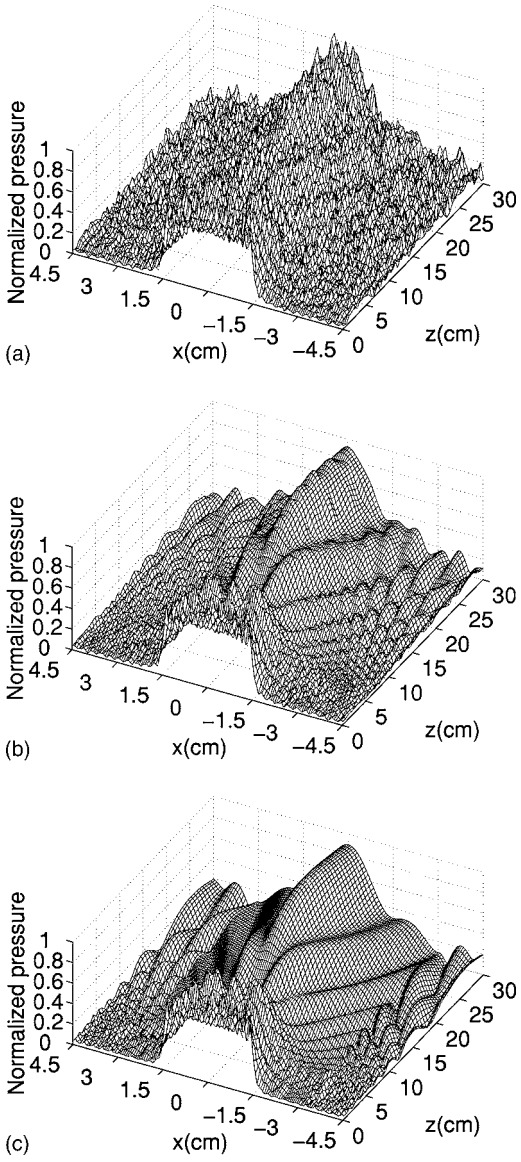

FIG. 3. Simulated pressure generated by a 3 cm × 3 cm square piston in nonattenuating media computed by the angular spectrum approach using (a) the spectral propagator without angular restriction, (b) the spectral propagator with angular restriction, and (c) the spatial propagator. The excitation frequency is 1 MHz. All fields are calculated in successive $D \times D$ transverse planes ($D=9$ cm), so the circular convolution errors generated by the spatial propagator are included.

edge of the computational grid, a discrete jump appears in the computed field. This error is an artifact of circular convolution between the spatial propagator and the velocity source, where the spatial propagator is evaluated on a $D \times D$ grid, and the dimension of the nonzero velocity source is $2a \times 2a$. All convolutions are performed over a $D \times D$ area with 2D FFTs to minimize the number of parameters needed to describe each simulation. If extra zero padding is used to enlarge both the $D \times D$ spatial propagator plane and the source plane, the circular convolution error is replaced with another error. With zero padding, as soon as the nonzero part of the velocity source is shifted to a location that overlaps with a value outside of the $D \times D$ rectangular window, the source is convolved with zero instead of the correct value of the spatial propagator. As a result, the pressure fields com-

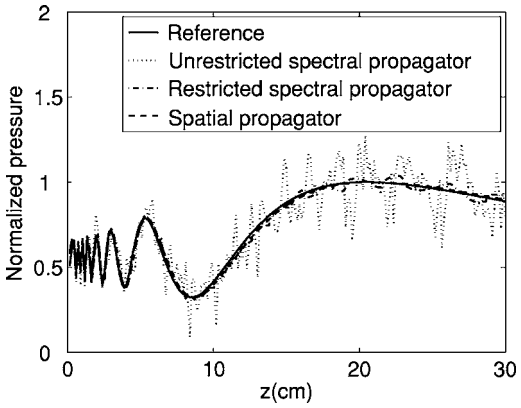

FIG. 4. Axial plots of the absolute value of the simulated complex pressure. Results are shown for the reference, the angular spectrum approach using the spectral propagator without and with angular restriction, and the spatial propagator.

puted with the spatial propagator are erroneous starting from a distance a from the edge. With or without zero padding, the errors due to the finite window applied to the spatial propagator always appear within a peripheral band of width a, but the $L \times L$ area in the center is not affected, where $L=D-2a$. In contrast, no such windowing error is present in the results from the spectral propagator, because the spectral propagator is analytically evaluated in the spatial frequency domain.

Figure 4 provides a more detailed comparison between the reference and the results in Figs. 3(a)–3(c) by highlighting the pressure variations in the axial direction where $x=y=0$. The axial pressure computed using the spectral propagator without angular restriction (dotted line) is corrupted by errors with high spatial frequencies. The field computed from the spectral propagator with angular restriction (dash-dot line) contains some intermediate frequency ripples. The field computed from the spatial propagator (dashed line) closely tracks the reference (solid line). Figure 4 emphasizes that the spatial propagator computes axial pressures more accurately than the spectral propagator in nonattenuating media.

In Fig. 5, the normalized root mean squared errors are calculated in three-dimensional volumes for different D values, where D represents the extent of the computational volume in both the x and the y directions. The results are plotted as a function of D, where the value of D ranges from 6 to 15 cm. The normalized root mean squared error curve for the spatial propagator (dashed line) is between that of the spectral propagator without angular restriction (dotted line) and with angular restriction (solid line). Thus, when the circular convolution errors produced by the spatial propagator are included, the spectral propagator with angular restriction achieves a smaller normalized root mean squared error.

In Fig. 5(b), the volumes are truncated at the edges to exclude the convolution errors, and then the normalized root mean squared errors are computed. The truncated volume has a lateral extent of $L \times L$, so the results are plotted as a function of L with $L=D-2a$, where L ranges from 3 to 12 cm. In Fig. 5(b), the errors from the spatial propagator are 2 to 4 times smaller than those in Fig. 5(a). The errors computed for the spectral propagator with and without angular restriction are influenced less by the truncation. The errors

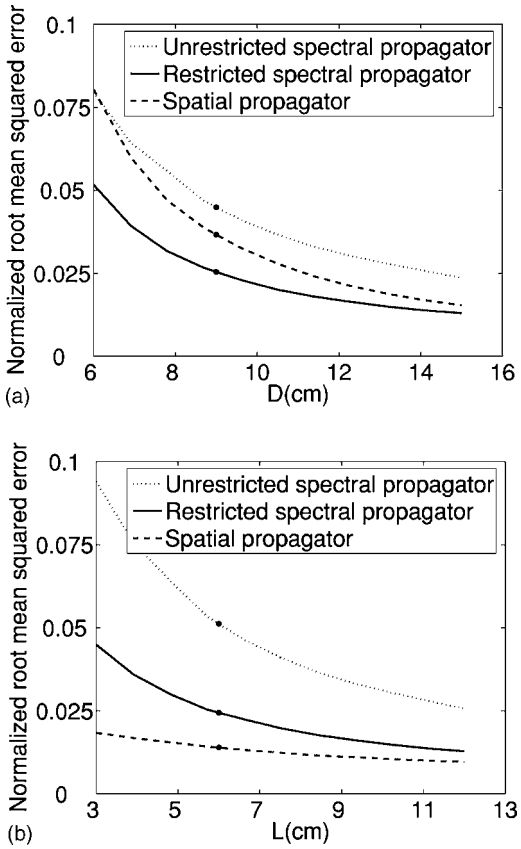

FIG. 5. Normalized root mean squared errors for the pressure generated by a uniform normal particle velocity distribution in nonattenuating media. The errors are evaluated in three-dimensional volumes where the lateral dimensions are (a) $D \times D$ and (b) $L \times L$ with $L=D-2a$. The markers on the curves indicate the corresponding results shown in Fig. 3.

without angular restriction are about 1.5 to 2 times higher than those with angular restriction in both Figs. 5(a) and 5(b). The difference between the dashed curves in Figs. 5(a) and 5(b) reinforces the need to truncate the field computed with the spatial propagator to exclude the errors produced at the edge of the grid.

B. Pressure calculations in attenuating media for a square piston with uniform normal particle velocity

When time-harmonic acoustic waves propagate in attenuating media, e.g., biological tissue, the angular spectrum approach either evaluates the spatial propagator with a complex wavenumber or applies the attenuation term $S(k_x,k_y,z)$ in Eq. (11) to the spectral propagator. Figure 6 shows the reference pressure generated by the same 3 cm $\times$ 3 cm square piston in attenuating media with $\alpha=1$ dB/cm/MHz. In Fig. 6, the reference pressure field attenuates quickly as z increases. The reference pressure is calculated with the fast near-field method[15] using 100 Gauss abscissas, which achieves 11 digits of accuracy compared to the result obtained with 2000 Gauss abscissas.

The pressures in attenuating media calculated by the angular spectrum approach in Fig. 7 are calculated with $D=9$ cm and then truncated to $L=6$ cm so that circular convolution errors are excluded from the spatial propagator result.

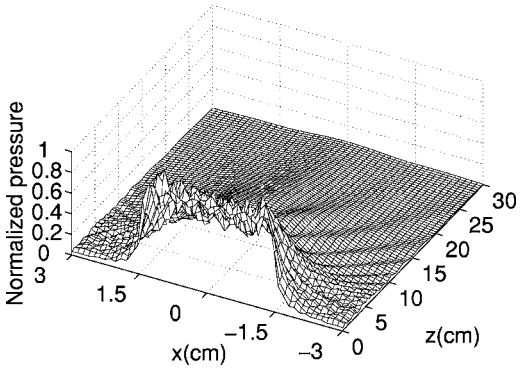

FIG. 6. The absolute value of the complex reference pressure generated by a 3 cm×3 cm square piston in attenuating media (α=1 dB/cm/MHz). The excitation frequency is 1 MHz and the normal velocity distribution is uniform across the piston surface. The reference pressure is computed with the fast near-field method.

Figure 7(a) shows the result for the spectral propagator without angular restriction. The field contains some high spatial frequency ripples due to undersampling in the spatial frequency domain. Figure 7(b) is calculated using the spectral propagator with angular restriction, and the ripples are reduced somewhat. Figure 7(c), which contains the result obtained with the spatial propagator, is relatively smooth. All three results are quite similar to the reference in Fig. 6. Therefore, the spectral propagator is preferable in attenuating media because the spectral propagator produces acceptable results in larger $D\times D$ transverse planes while the spatial propagator only gives accurate results in smaller $L\times L$ transverse planes. Meanwhile, the spectral propagator uses less computation time because fewer FFT computations are required.

Figure 8 shows the normalized root mean squared errors obtained using the spectral propagator (with and without angular restriction) and the spatial propagator. The pressures are calculated in $D\times D$ transverse planes and then truncated to $L\times L$ with $L=D-2a$. The normalized root mean squared error is then computed in the truncated volume. In Fig. 8, L ranges from 3 to 12 cm, and the three curves approximately converge to the same value for large L. The difference between the dotted and the solid curves is smaller in Fig. 8 than in Fig. 5(b), which implies that angular restriction is less important in attenuating media. This occurs because $S(k_x,k_y,z)$ is a low-pass filter that effectively attenuates the high spatial frequency components in $H_u(k_x,k_y,z)$. Since the attenuation reduces the highly oscillatory spectrum near $k_x^2+k_y^2=k^2$, aliasing errors in attenuating media are less severe than those in nonattenuating media, therefore angular restriction is not required in attenuating media.

C. Pressure calculations in nonattenuating media for a square piston with apodized normal particle velocity

The distribution of the normal particle velocity on the piston surface also influences the numerical accuracy of the angular spectrum approach. To demonstrate the effect of apodization, a tapered window is applied to the aperture. The

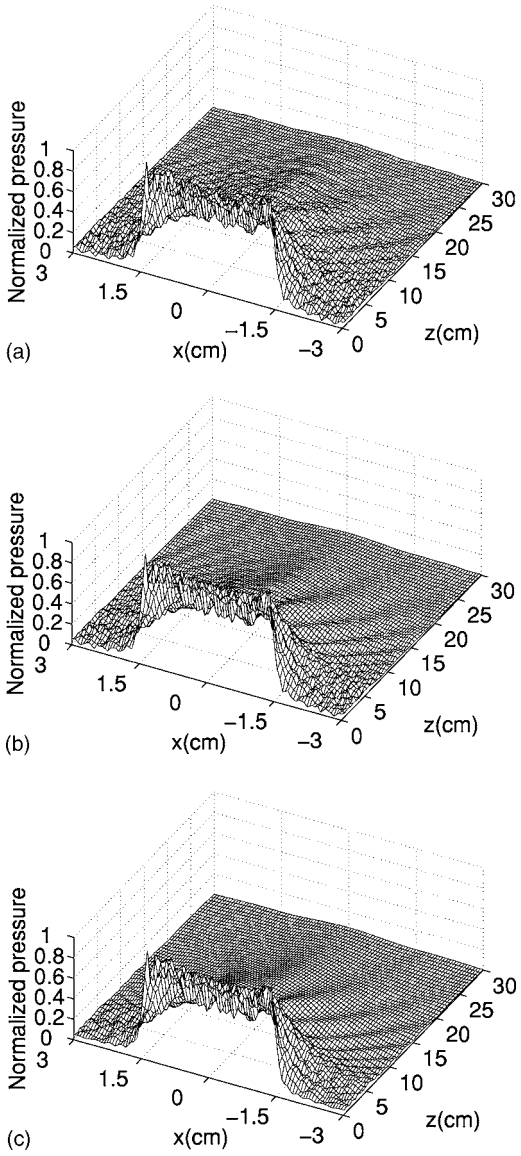

FIG. 7. The absolute value of the simulated complex pressure in attenuating media computed with the angular spectrum approach using (a) the spectral propagator without angular restriction, (b) the spectral propagator with angular restriction, and (c) the spatial propagator. All fields are calculated in successive $D\times D$ transverse planes (D=9 cm) and truncated to $L\times L$ (L=6 cm), where $L=D-2a$.

apodization function evaluated here is a product of quadratic polynomials in both the x and the y directions, where

$$u(x,y)=\begin{cases}\left[1-\left(\frac{x}{a}\right)^2\right]\left[1-\left(\frac{y}{b}\right)^2\right], & |x|<a,\ |y|<b\\ 0, & |x|\geqslant a,\ |y|\geqslant b.\end{cases} \tag{13}$$

This source velocity has a peak at the origin and smoothly decays to zero at the edges of the piston. The pressure from the apodized piston is calculated with point source superposition applied to the Rayleigh–Sommerfeld integral,[16] where each of the point sources is weighted by the value of the normal velocity at the subelement center. In the numerical evaluation of the Rayleigh–Sommerfeld integral, the reference field is computed with 5000×5000 uniform subdivi-

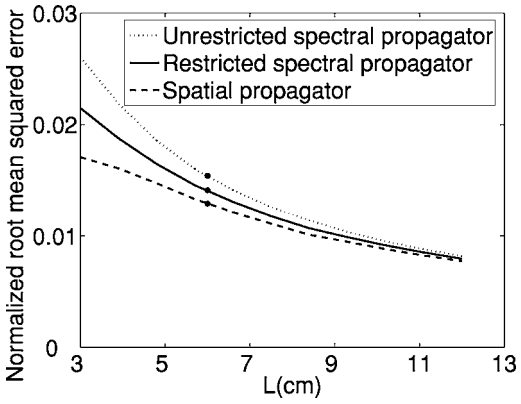

FIG. 8. Normalized root mean squared errors for the pressure generated in attenuating media (α=1 dB/cm/MHz) by a 3 cm×3 cm uniformly excited square piston. The errors are evaluated in three-dimensional volumes where the lateral dimensions are $L\times L$ with $L=D-2a$. The markers on the curves indicate the corresponding results shown in Fig. 7.

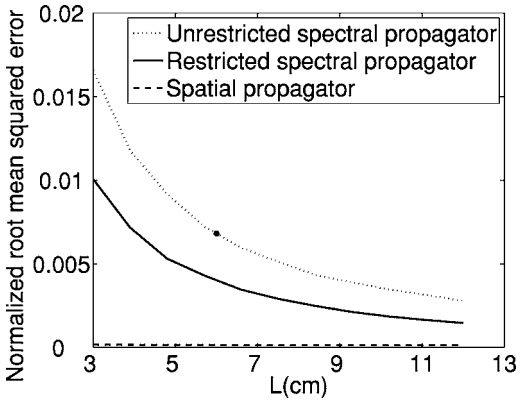

FIG. 10. Normalized root mean squared errors for the pressure generated in nonattenuating media by a 3 cm×3 cm square piston with an apodized normal particle velocity distribution. The errors are evaluated in three-dimensional volumes where the lateral dimensions are $L\times L$ with $L=D-2a$. The marker on the dotted line indicates the result in Fig. 9(b).

sions on the piston surface. This reference is accurate to 7 digits, as determined from a comparison with the same result calculated with 10 000×10 000 subdivisions. Figure 9(a) shows the reference field in the $y=0$ plane computed in nonattenuating media. The angular spectrum approach then computes the 3D field generated by a rectangular piston with an apodized source profile. Figure 9(b) shows the pressure computed by the angular spectrum approach using the spectral propagator without angular restriction. The results obtained using the spectral propagator with angular restriction and from the truncated spatial propagator are very similar to Fig. 9(b) and are therefore not shown.

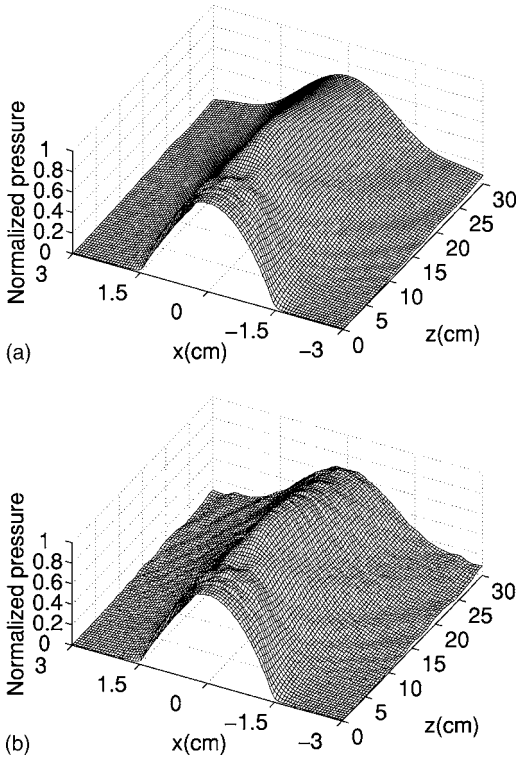

FIG. 9. The absolute value of the simulated complex pressure in nonattenuating media generated by a 3 cm×3 cm square piston with apodized normal particle velocity distribution. (a) The reference pressure and (b) the pressure computed by the spectral propagator without angular restriction. The excitation frequency is 1 MHz.

Figure 10 shows the normalized root mean squared errors of the pressures computed with the spectral propagator (with and without angular restriction) and the spatial propagator. The pressures are calculated in a 3D volume with $D\times D$ lateral extent, then the volume is truncated in the lateral directions to $L\times L$ with $L=D-2a$ and the normalized root mean squared error is evaluated. The errors in all three curves are much lower than those computed with the uniform velocity source in nonattenuating media [Fig. 5(b)] or attenuating media (Fig. 8). The uniform velocity distribution corresponds to a source spectrum that is represented by a 2D sinc function with large sidelobes. The spatial frequencies in the sidelobes of the sinc function leak into the pressure field and cause errors in the near field, as shown in Figs. 3(a), 3(b), 7(a), and 7(b). In contrast, the apodized piston has a tapered velocity distribution, the spectrum of which has lower sidelobes and is therefore less prone to high spatial frequency errors. The source spectrum along the k_x direction where $k_y=0$, contains first sidelobes at −6.8 and −11.2 dB for the uniform velocity distribution and the apodized velocity distribution, respectively. Near $k_x=k$ and $k_y=0$, where the spectrum becomes evanescent outside of this range, the sidelobes are −17.7 and −30.8 dB, for the uniform and the apodized velocity distributions, respectively. Thus, by reducing the sidelobe levels in the source spectrum, apodization achieves significant reduction in the error and eliminates the need for angular restriction.

IV. DISCUSSION

A. Reference pressure calculations

The reference fields for the uniformly excited piston are computed with the fast near-field method.[15] Previous calculations have demonstrated that the fast near-field method, the impulse response method,[17] and other integral methods converge to the same result when the number of abscissas is very large.[15] Overall, the fast near-field method provides the most accurate results in the shortest time for numerical calculations in the near-field region. For example, the fast near-

field method takes 19 min to compute the pressure in a $201\times201\times200$ grid and is accurate to 11 digits. A 500×500 point source superposition calculation with the Rayleigh–Sommerfeld integral for the same uniform velocity distribution on the same grid takes 40 min and is only accurate to 4 digits. These computation times are evaluated on a Pentium 4 PC with 4 Gbytes memory running the Windows XP operating system. All routines are written in C and executed with MATLAB 7.0. The FFT calculations are computed with FFTW library version 3.1.2.

B. Error and time trade-offs

Computations with the spatial propagator take longer than calculations with the spectral propagator because an extra 2D FFT calculation is needed in each plane to convert the spatial propagator into the spatial frequency domain. Simulations of the pressure generated by the 3 cm $\times$ 3 cm piston with N ranging from 301 to 1024 show that the computation time for the spatial propagator is 1.1–1.9 times that for the spectral propagator. This ratio approaches the smaller value as N increases. For example, after the pressure is calculated with $N=301$ ($D=9$ cm), the field is truncated to a $201\times201\times200$ grid (6 cm $\times$ 6 cm $\times$ 30 cm volume) for error evaluations. The spectral propagator computes the complex pressure in 15.22 s with a normalized root mean squared error of 2.45%, and the spatial propagator computes the result in 28.90 s with a normalized root mean squared error of 1.39%. When $N=512$ ($D=15.33$ cm), the angular spectrum approach evaluated with the spectral propagator computes the 3D grid of complex pressures with a normalized root mean squared error of 1.47% in 1.23 min, whereas the spatial propagator takes 1.99 min using the same parameters while achieving a normalized root mean squared error of 1.38%. As the computational grid becomes larger, the difference between the spatial and spectral propagator becomes smaller in terms of both error and time.

Overall, the spectral propagator computes pressures faster than the spatial propagator in the same grid. Furthermore, the spatial propagator evaluated in a $D\times D$ plane yields accurate results only in an $L\times L$ plane, where $L=D-2a$, while the spectral propagator produces useful results in the entire $D\times D$ plane using the same $N\times N$ grid with $N=D/\delta+1$. The spatial propagator generates more accurate results than the spectral propagator in nonattenuating media, whereas the two propagators achieve similar accuracies for simulations in attenuating media or for an apodized velocity source. Therefore, the spectral propagator is preferred if the computational grid is large and time is a limiting factor (for example, when a large number of these calculations are performed in a parametric simulation). When the numerical accuracy is the primary consideration, the spatial propagator is preferred, especially in nonattenuating media.

C. Error sources for the spectral propagator

The spectral propagator is an analytical function, but the numerical implementation discretizes the spectral propagator by multiplying the continuous spectrum with $\mathrm{comb}(k_x/\Delta k, k_y/\Delta k)$, where $\Delta k=2\pi/(N\delta)$. The resulting spatial pressure distribution is therefore shifted and added in blocks of size $D\times D$. Since the analytical inverse Fourier transform of the spectral propagator extends to ± infinity in the spatial domain, the tails from all of the other blocks leak into the central $D\times D$ area and cause aliasing errors as shown in Fig. 3(a).

The nonzero portion of the spectral propagator is mostly confined within $k_x^2+k_y^2\leqslant k^2$, and the undersampling of the spectral propagator can be severe as $\sqrt{k_x^2+k_y^2}$ approaches k. In Eq. (6), two terms contain $\sqrt{k^2-k_x^2-k_y^2}$, where one is found in the exponential phase term, and the other is in the denominator. The real and imaginary parts of the numerator oscillate more rapidly as k_x and k_y approach $k_x^2+k_y^2=k^2$. Meanwhile, the value of the denominator decays quickly until the singularity is encountered at $k_x^2+k_y^2=k^2$. Both of these phenomena lead to numerical difficulties in terms of spectral sampling. The high spatial frequency components are reduced by applying a low-pass filter to $H_u(k_x,k_y,z)$ either through angular restriction or attenuation, and the same effect is achieved by filtering the source spectrum through apodization. In an effort to address the problem with singularities in $H_u(k_x,k_y,z)$ at $k_x^2+k_y^2=k^2$, different values were substituted for the infinite value encountered in this location, including 0, the amplitude of an adjacent point, and an average value of the adjacent points around the singularity.[14] Each of these strategies produces very similar errors. This suggests that the numerical singularities at $k_x^2+k_y^2=k^2$ have little influence on the overall error, especially when evaluated in the contexts of angular restriction, attenuation, or apodization.

D. Error sources for the spatial propagator

The spatial propagator $h_u(x,y,z)$ is smooth everywhere except at locations adjacent to the radiator, i.e., less than 1 wavelength from the piston surface, and the only singularity occurs on the piston surface at (0,0,0). Away from the piston surface, the Nyquist sampling rate of the spatial propagator is easily satisfied when $\delta\leqslant\lambda/2$ is the sampling interval.[3] The analytical representation of the spatial propagator extends to ± infinity in both the x and the y directions. However, the spatial propagator is truncated by a $D\times D$ window in angular spectrum calculations. When this truncated propagator is convolved with a velocity source of size $2a\times2a$ using 2D FFTs, circular convolution errors will appear in a band of width a along each edge as shown in Fig. 3(a). If the $D\times D$ plane is enlarged with zero padding, the circular convolution error is replaced with the windowing error due to the truncation of the spatial propagator. In other words, the pressure field that excludes the erroneous boundary is always $L\times L$, where $L=D-2a$, with or without zero padding.

V. CONCLUSION

The performance of spatial and spectral propagators applied to the angular spectrum approach is evaluated for near-field pressure simulations with a square piston. Calculations with the spatial propagator are performed in a $D\times D$ plane, and results show that the $L\times L$ portion at the center (with $L=D-2a$) contains accurate results, whereas the peripheral band of width a consistently contains errors with or without

zero padding. Therefore, the edge region computed with the spatial propagator should always be discarded. When the spectral propagator is used, undersampling in the spatial frequency domain causes errors in the computed pressure fields, and these are reduced in nonattenuating media by angular restriction. In attenuating media or when the source is apodized, the errors produced by the spatial propagator and the spectral propagator (with and without angular restriction) are small, and the difference between the spatial and spectral propagators is negligible. Meanwhile, the spatial frequency filtering effect of attenuation or apodization reduces the aliased components, and the need for angular restriction is eliminated in these cases. The spatial propagator, which only yields accurate results in planes of size $L \times L$, requires more calculation time than the spectral propagator. Thus, the spatial and spectral propagator each has distinct advantages and disadvantages that depend on the grid size, the attenuation value, and the source velocity distribution, and these determine the trade-offs between the numerical accuracy and the computation time for angular spectrum calculations.

ACKNOWLEDGMENTS

This work was supported in part by NIH R01CA093669, NIH R21CA121235, and NSF Theoretical Foundations Grant No. 0634786.

[1]J. W. Goodman, *Introduction to Fourier Optics*, 2nd ed. (McGraw-Hill, New York, 1996).
[2]G. T. Clement and K. Hynynen, "Field characterization of therapeutic ultra-sound phased arrays through forward and backward planar projection," J. Acoust. Soc. Am. **108**, 441–446 (2000).
[3]D. P. Orofino and P. C. Pedersen, "Efficient angular spectrum decomposition of acoustic sources. I. Theory," IEEE Trans. Ultrason. Ferroelectr. Freq. Control **40**, 238–249 (1993).
[4]D. P. Orofino and P. C. Pedersen, "Efficient angular spectrum decomposition of acoustic sources. II results," IEEE Trans. Ultrason. Ferroelectr. Freq. Control **40**, 250–257 (1993).
[5]P. R. Stepanishen and K. C. Benjamin, "Forward and backward projection of acoustic fields using FFT methods," J. Acoust. Soc. Am. **71**, 803–812 (1982).
[6]P. Wu, R. Kazys, and T. Stepinski, "Analysis of the numerically implemented angular spectrum approach based on the evaluation of two-dimensional acoustic fields. I. Errors due to the discrete Fourier transform and discretization," J. Acoust. Soc. Am. **99**, 1339–1348 (1996).
[7]P. Wu, R. Kazys, and T. Stepinski, "Analysis of the numerically implemented angular spectrum approach based on the evaluation of two-dimensional acoustic fields. II. Characteristics as a function of angular range," J. Acoust. Soc. Am. **99**, 1349–1359 (1996).
[8]P. Wu, R. Kazys, and T. Stepinski, "Optimal selection of parameters for the angular spectrum approach to numerically evaluate acoustic fields," J. Acoust. Soc. Am. **101**, 125–134 (1997).
[9]P. Wu and T. Stepinski, "Extension of the angular spectrum approach to curved radiators," J. Acoust. Soc. Am. **105**, 2618–2627 (1999).
[10]P. T. Christopher and K. J. Parker, "New approaches to the linear propagation of acoustic fields," J. Acoust. Soc. Am. **90**, 507–521 (1991).
[11]D. Liu and R. C. Wagg, "Propagation and backpropagation for ultrasonic wavefront design," IEEE Trans. Ultrason. Ferroelectr. Freq. Control **44**, 1–13 (1997).
[12]R. J. Zemp and J. T. Tavakkoli "Modelling of nonlinear ultrasound propagation in tissue from array transducers," J. Acoust. Soc. Am. **113**, 139–152 (2003).
[13]E. G. Williams, *Fourier Acoustics: Sound Radiation and Nearfield Acoustical Holography* (Academic, London, 1999).
[14]E. G. Williams and J. D. Maynard, "Numerical evaluation of the Rayleigh integral for planar radiators using the FFT," J. Acoust. Soc. Am. **72**, 2020–2030 (1982).
[15]R. J. McGough, "Rapid calculations of time-harmonic nearfield pressures produced by rectangular piston," J. Acoust. Soc. Am. **115**, 1934–1941 (2004).
[16]J. Zemanek, "Beam behavior within the nearfield of a vibrating piston," J. Acoust. Soc. Am. **49**, 181–191 (1971).
[17]J. C. Lockwood and J. G. Willette, "High-speed method for computing the exact solution for the pressure variations in the nearfield of a baffled piston," J. Acoust. Soc. Am. **53**, 735–741 (1973).